Tailoring propagation of light via spin-orbit interactions in correlated disorder

Federico Carlini [1,2] and Nicolas Cherroret [1]

[1]*Laboratoire Kastler Brossel, Sorbonne Université, CNRS, ENS-PSL Research University, Collège de France, 4 Place Jussieu, 75005 Paris, France*

[2]*MajuLab, International Joint Research Unit UMI 3654, CNRS, Université Côte d'Azur, Sorbonne Université, National University of Singapore, Nanyang Technological University, Singapore*

Based on the fundamental interplay between spatial wavefronts and polarization degrees of freedom, spin-orbit interactions (SOI) of light constitute a novel tool for optical control at the nanoscale. While well described in simple geometries, SOI of light in disordered environments, where only a partial knowledge of the material's microscopy is available, remain largely unexplored. Here, we show that in transversally random media the disorder correlation can be exploited to tailor a variety of trajectories for ballistic beams via SOI. In particular, we show the existence of an oscillating spin Hall effect, stemming from the deformation of the phase of the wavefront due to SOI. In combination with a weak measurement, this phenomenon can also be maximized by an optimal choice of the disorder correlation.

I. INTRODUCTION

Spin-orbit interactions of light refer to the interplay between the polarization and wavefront of optical beams, usually encoded in spin and orbital angular momenta. This mechanism is attracting a lot of attention as it brings about a vast number of potential applications in the control of light at the nanoscale, the optical manipulation of small objects or for metrology purposes in nanostructures (see [1–3] for recent reviews). A particular manifestation of SOI of light is the optical spin Hall effect (SHE), an analog of the electronic spin Hall effect that lies at the core of spintronics [4,5]. In optics, the SHE describes transverse beam shifts occurring at a subwavelength scale [6]. Although naturally small, SHEs have been observed at interfaces using weak-measurement methods [7–9], in glass cylinders exploiting multiple reflection [10], or in nonparaxial configurations [11–13]. An important class of systems exhibiting SHEs are inhomogeneous materials. A seminal example is gradient-index media: while geometrical optics predicts that beam trajectories are not affected by polarization, at the wave level circularly polarized beams experience helicity-dependent transverse shifts [14,15]. Akin to the electronic SHE where the electron spin couples to a potential gradient, in optics the photon helicity couples to the refractive-index gradient, a mechanism that can be interpreted in terms of geometric Berry phase [16,17].

Beyond the case of a controlled inhomogeneity, it was recently shown that a SHE of light could also emerge for beams propagating in transversally disordered media [18]. In practice, clarifying the role of SOI in disordered environments is important for at least two reasons. First, disordered materials are in general more the rule than the exception, in particular at the nanoscale where SOI typically operate. In addition, recent progresses in wave control or imaging have shown the great

potential of treating disorder as a tool rather than as a nuisance in general [19–24]. Whether this potential could be pushed to the realm of spin-orbit physics remains an open question. In this article, we take a step in that direction by theoretically showing that the combined influence of SOI on the amplitude and the phase of the optical wavefront can be exploited to tailor a variety of transverse motions for the ballistic component of light in a disordered medium, the so-called coherent mode. This control relies on two fundamental ingredients, neglected in [18], the disorder correlation and the random variations of the refractive index. In particular, we find that a proper choice of the disorder correlation makes it possible to realize an *oscillating* SHE, see Fig. 1, and a corresponding oscillation of the beam polarization. This phenomenon, a consequence of the interferential nature of the coherent mode, was not previously known. Remarkably, while such an oscillating SHE is naturally small and may be hidden by multiple scattering, we show that these drawbacks can be both overcome. First, by a weak-measurement detection scheme allowing one to amplify SOI of light to the macroscopic level and, second, by a proper tuning of the disorder correlation to minimize the propagation distance at which the SHE occurs.

II. THE MODEL

Consider a monochromatic, polarized optical field $\boldsymbol{E}_0(\boldsymbol{r}_\perp) = E_0(\boldsymbol{r}_\perp)\boldsymbol{e}_0$ impinging at $z = 0$ on a three-dimensional material lying in the half-plane $z > 0$ [$\boldsymbol{r}_\perp = (x, y)$]. We choose $E_0(\boldsymbol{r}_\perp) = [2/(\pi w_0^2)]^{1/2} \exp(-r_\perp^2/w_0^2 + ik_0 x)$ with $k_0 w_0 \gg 1$, which describes a tilted, collimated beam of waist w_0, as illustrated in Fig. 1(a). The polarization vector lies in the (x', y) plane, perpendicular to the direction of propagation. We take it to be of the form $\boldsymbol{e}_0 = (\hat{\boldsymbol{x}}' + e^{i\phi}\hat{\boldsymbol{y}})/\sqrt{2}$. We focus on a dielectric
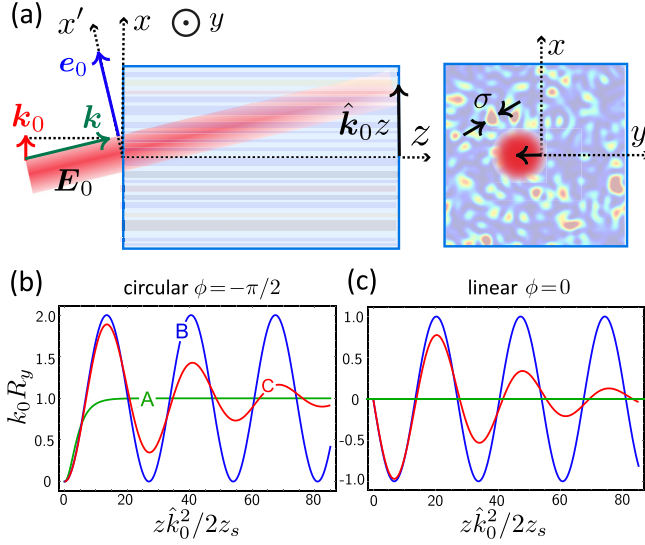
FIG. 1. (a) Propagation of a tilted beam of transverse wave vector $\boldsymbol{k}_0 = k_0\hat{\boldsymbol{x}}$ in a medium disordered in plane (x, y) (correlation length σ). At a distance z, the beam centroid along x is $\hat{k}_0 z$. Due to spin-orbit interactions, the beam also has a transverse motion $R_y(z)$ along y (spin Hall effect). (b) $R_y(z)$ for circularly polarized incident light ($\phi = -\pi/2$), at $\hat{k}_0 = 0.1$. The three trajectories correspond to the points A ($k_0\sigma = 0.62286$), B ($k_0\sigma = 0.8749$), and C ($k_0\sigma = 0.84$) in Fig. 2, where SOI respectively affect only the amplitude ($z_L = \infty$), only the phase ($z_S = \infty$), and both the phase and amplitude ($z_{L/S}$ finite) of the wavefront. In cases B and C, a SHE oscillating around k_0^{-1} appears. (c) For a beam linearly polarized at 45° in the plane (x', y) ($\phi = 0$), a SHE is also present but oscillates around 0.

medium with transverse spatial disorder: its permittivity $\epsilon(\boldsymbol{r}_\perp) = \bar{\epsilon} + \delta\epsilon(\boldsymbol{r}_\perp)$ has a random component $\delta\epsilon$ in the plane (x, y), but is homogeneous along z [25–27]. In practice, this geometry can be realized using two-dimensional photonic lattices imprinted onto a photorefractive crystal [25,26] or a glass [28]. We model the disorder fluctuations by a random function of zero mean and Gaussian correlation, $\langle\delta\epsilon(\boldsymbol{r}_\perp)\delta\epsilon(0)\rangle = \gamma/(4\pi\sigma^2)\exp(-r_\perp^2/4\sigma^2)$, where γ is the disorder amplitude, σ the correlation length, and the brackets refer to disorder averaging.

As the beam propagates in the medium, the components E_j ($j = x, y, z$) of the electric field obey

$$\left[\left(\Delta + \omega^2\epsilon(\boldsymbol{r}_\perp)/c_0^2\right)\delta_{ij} - \nabla_i\nabla_j\right]E_j(\boldsymbol{r}_\perp, z) = 0, \quad (1)$$

with ω the carrier frequency and c_0 the vacuum speed of light. In this article, we study the evolution of the coherent mode, of intensity distribution $I_c(\boldsymbol{r}_\perp, z) = |\langle\boldsymbol{E}(\boldsymbol{r}_\perp, z)\rangle|^2$, after a propagation distance z. The coherent mode refers to the portion of light propagating ballistically in the medium, i.e., in the forward direction $\hat{\boldsymbol{x}}$, as opposed to light undergoing multiple scattering [29]. To access this intensity distribution, we examine the Fourier components of the average field. The latter are formally given by $\langle\tilde{\boldsymbol{E}}(\boldsymbol{k}_\perp, z)\rangle = \exp(ik_z z - i\boldsymbol{\Sigma}z/2k_z)\tilde{\boldsymbol{E}}_0(\boldsymbol{k}_\perp)$, where $\tilde{\boldsymbol{E}}_0(\boldsymbol{k}_\perp) = \sqrt{2\pi}w_0\exp[-(\boldsymbol{k}_\perp - \boldsymbol{k}_0)^2w_0^2/4]$ is the field momentum distribution at the interface $z = 0$ and $k_z = \sqrt{k^2 - k_\perp^2}$, with $k = \sqrt{\bar{\epsilon}}\omega/c_0$ the total wave number. The quantity $\boldsymbol{\Sigma}$, known as the self-energy tensor [29], encodes all

effects of the disorder. Its real part describes how the phase of the wavefront evolves on average in the disorder (mean refractive index), while its imaginary part governs the attenuation of its amplitude (extinction coefficient). An explicit calculation detailed in Appendix A gives

$$\langle\tilde{\boldsymbol{E}}(\boldsymbol{k}_\perp, z)\rangle = \tilde{E}_0(\boldsymbol{k}_\perp)e^{ik_z z}[e^{-i\Sigma_1 z/2k_z}\boldsymbol{e}_0$$
$$+ (e^{-i\Sigma_2 z/2k_z} - e^{-i\Sigma_1 z/2k_z})\boldsymbol{p}(\boldsymbol{k}_\perp)]. \quad (2)$$

The complex numbers Σ_1 and Σ_2, evaluated below, are combinations of eigenvalues of $\boldsymbol{\Sigma}$. The existence of two independent self-energies here stems from the fact that as soon as the incident beam is tilted, i.e., $k_0 \neq 0$, the statistical isotropy in the plane perpendicular to the direction of propagation is broken, making momentum conservation along z (due to translation invariance along that direction) the unique symmetry of the problem. In Eq. (2), the first term in the right-hand side (r.h.s.) describes an evolution *without* spatial deformation. Its amplitude is controlled by Σ_1, which defines the mean free path along z, $z_s = -k_z/\text{Im}(\Sigma_1)$, beyond which the coherent mode is attenuated due to scattering in other directions [27,29]. The second term in the r.h.s. is proportional to the projection $\boldsymbol{p}(\boldsymbol{k}_\perp) = (\hat{\boldsymbol{e}}_\perp \cdot \boldsymbol{e}_0)\hat{\boldsymbol{e}}_\perp + (\hat{\boldsymbol{z}} \cdot \boldsymbol{e}_0)\hat{\boldsymbol{z}}$ of the polarization onto the $(\hat{\boldsymbol{e}}_\perp = \boldsymbol{k}_\perp/k_\perp, \hat{\boldsymbol{z}})$ plane. It describes a wavefront deformation coupling polarization and momentum and, as such, encodes the phenomenon of spin-orbit interaction. Notice that this deformation only arises when $\Sigma_1 \neq \Sigma_2$.

III. CENTROID EVOLUTION

To show the effect of the SOI term in Eq. (2), we examine the beam centroid, defined as

$$\langle\boldsymbol{R}(z)\rangle = \frac{\int d\boldsymbol{r}_\perp \boldsymbol{r}_\perp I_c(\boldsymbol{r}_\perp, z)}{\int d\boldsymbol{r}_\perp I_c(\boldsymbol{r}_\perp, z)}. \quad (3)$$

The first term in the r.h.s. of Eq. (2) gives the main contribution to this quantity: $\langle\boldsymbol{R}(z)\rangle \simeq \hat{\boldsymbol{k}}_0 z$. This result features a straight-line propagation with fixed polarization; see Fig. 1(a). It also coincides with the prediction of the paraxial limit, where $\hat{k}_0 = k_0/k \ll 1$. Indeed, at small angle one finds $\Sigma_1 - \Sigma_2 = O(\hat{k}_0^2) \to 0$, so that statistical isotropy in the (x', y) is restored and the second term in Eq. (2) vanishes. In general, however, Σ_1 and Σ_2 differ, leading to a nontrivial component $R_y(z)$ of $\langle\boldsymbol{R}(z)\rangle$ along the *transverse* direction y [30]. Indeed, inserting Eq. (2) into Eq. (3) we find

$$R_y(z) = -\frac{\sin\phi}{k_0}\left[1 - \frac{\cos z/2z_L}{\cosh z/2z_S}\right] + \frac{\cos\phi}{k_0}\frac{\sin z/2z_L}{\cosh z/2z_S}. \quad (4)$$

This transverse motion is governed by two core parameters, $z_S = [\text{Im}(\Sigma_2 - \Sigma_1)/k_z]^{-1}$ and $z_L = [\text{Re}(\Sigma_2 - \Sigma_1)/k_z]^{-1}$, which represent respectively the length scales over which SOI modify the amplitude and the phase of the coherent mode. The first term in Eq. (4) was originally discovered in [18], for an elementary model of uncorrelated disordered and discarding refractive-index effects [i.e., $\text{Re}(\Sigma_1), \text{Re}(\Sigma_2) = 0$]. Under these approximations, $z_L \to \infty$ and $z_S \to z_s/\hat{k}_0^2$, so that $R_y(z) = -\sin\phi/k_0[1 - \cosh^{-1}(z\hat{k}_0^2/2z_s)]$. This describes a monotonic shift existing only for beams of finite helicity (or spin) $\sin\phi$. In the more realistic case considered here, however, the physics pertaining to Eq. (4) is much richer
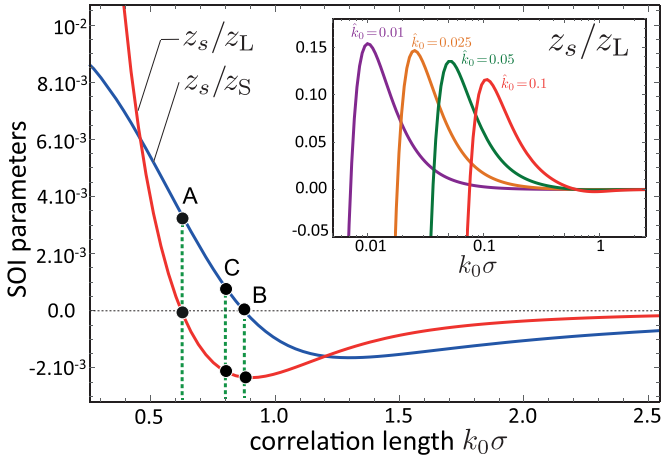
FIG. 2. Length scales z_L and z_S controlling the SHE as a function of the disorder correlation length, for $\hat{k}_0 = 0.1$ and in units of the mean free path z_s. At points A and B, $z_L = \infty$ and $z_S = \infty$, respectively. At point C, both z_S and z_L are finite. The inset shows that z_s/z_L reaches a maximum at lower correlation lengths. At this maximum, the oscillating SHE occurs at the scale of a few z_s.

since the modifications of the refractive index due to SOI give rise to spatial *oscillations* of the beam at the scale of z_L, modulating a monotonic component governed by z_S. In Eq. (2), these oscillations originate from the interference between the SOI term and itself, and between the SOI term and the paraxial one.

Both z_S and z_L are functions of $\hat{k}_0$, the deviation from paraxiality, and σ, the disorder correlation. We have computed them from Σ_1 and Σ_2; see Appendix B for the exact analytical expressions. The results, shown in Fig. 2, reveal the interesting feature that z_L^{-1} and z_S^{-1} vanish at specific values of $k_0\sigma$ (points A and B, respectively). In practice, this offers the possibility to tailor various types of SHEs via σ. To illustrate this idea, we show in Fig. 1(b) and 1(c) the transverse motion realized for $\phi = -\pi/2$ and 0 at points A and B, as well as at point C where both z_S and z_L are finite. In configuration A, SOI only affect the amplitude of the wavefront. This leads to a monotonic increase of $R_y(z)$ toward the asymptotic value $1/k_0$ for $z \gg z_S$, effectively reproducing the result of [18]. In case B, in contrast, SOI are purely of phase origin, and $R_y(z)$ exhibits oscillations around $1/k_0$. In the generic case C, finally, the oscillations are present but damped. Another interesting prediction of Eq. (4) is that an oscillating SHE can arise even for linearly polarized beams ($\phi = 0$), i.e., without initial spin; see Fig. 1(c). We will come to this intriguing phenomenon below.

IV. POLARIZATION EVOLUTION

The SHE of the coherent mode is accompanied by an evolution of its mean polarization direction $\boldsymbol{e}(z)$. The latter follows from Eq. (2), using the fact that the momentum distribution of the beam always remains peaked around $\boldsymbol{k}_0$: $\boldsymbol{e}(z) \simeq \langle \tilde{\boldsymbol{E}}(\boldsymbol{k}_0, z)\rangle / |\langle \tilde{\boldsymbol{E}}(\boldsymbol{k}_0, z)\rangle|$, with

$$\langle \tilde{\boldsymbol{E}}(\boldsymbol{k}_0, z)\rangle \propto [e^{-i\Sigma_2 z/2k_z}\hat{\boldsymbol{x}}' + e^{i\phi}e^{-i\Sigma_1 z/2k_z}\hat{\boldsymbol{y}}]. \quad (5)$$
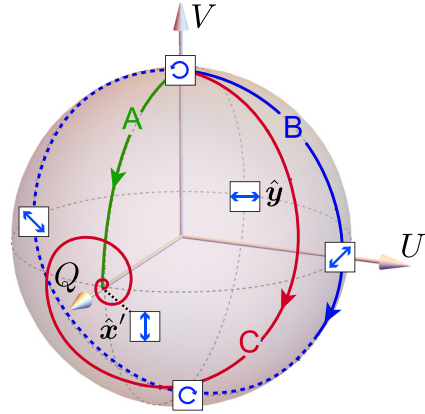

FIG. 3. Evolution of the polarization state $\boldsymbol{e}(z)$ on the Poincaré sphere when starting from a circularly polarized beam ($\phi = \pi/2$), in configurations A, B, and C. Axes are parametrized by the Stokes parameters U, V, and Q.

Equation (5) showcases the breaking of statistical isotropy when $\Sigma_1 \neq \Sigma_2$. It also indicates that SOI naturally imprint *birefringence* to the random medium. From Eq. (5), we infer

$$\boldsymbol{e}(z) = \frac{\hat{\boldsymbol{x}}' + e^{i\phi + iz/2z_L}e^{-z/2z_S}\hat{\boldsymbol{y}}}{\sqrt{1 + e^{-z/z_S}}}, \quad (6)$$

whose evolution is represented on the Poincaré sphere of Fig. 3 for a circularly polarized beam, in the three configurations discussed above. In case A, the polarization directly turns from circular to linear following the shortest path on the Poincaré sphere. In contrast, in configuration B the oscillating SHE is associated with a permanent, periodic evolution of the helicity. In the generic case C, finally, the oscillation of helicity is damped and $\boldsymbol{e}(z \gg z_S)$ converges to the attractor point $\hat{\boldsymbol{x}}'$. Fundamentally, the dual evolutions of $R_y(z)$ and $\boldsymbol{e}(z)$ originate from the conservation of angular momentum

$$k_0 R_y(z) + V(z) = \text{constant} = V(0) = \sin\phi. \quad (7)$$

In this relation, $V(z) = 2\int d\boldsymbol{r}_\perp \text{Im}(\langle E_x^*\rangle\langle E_y\rangle)/\int d\boldsymbol{r}_\perp I_c$ is the spin angular momentum (i.e., the amount of circularly polarized light in the beam, V axis in Fig. 3) and $k_0 R_y(z)$ is the beam orbital momentum, with Eq. (7) implying a mutual conversion between the two [31]. For $\phi = \pi/2$ and in case A, the initial spin is monotonically converted into orbital momentum while the beam is monotonically shifted. In cases B and C, in contrast, the exchange between V and R_y involves successive mutual conversions, hence the periodic trajectories. Together with Eq. (5), the conservation of angular momentum also sheds light on the second term in Eq. (4), which predicts a SHE for a spinless incident beam, $V(0) = 0$. In that case, the beam *spontaneously* acquires a finite spin thanks to the birefringence effect, Eq. (5). A transverse motion then spontaneously appears, satisfying Eq. (7). Interestingly, the SOI birefringence resembles the magneto-optic Voigt (or Cotton-Mouton) effect, where a magnetic field perpendicular to the direction of propagation converts a linear polarization into an elliptic one [32]. In our scenario, the role of the magnetic field is played by $\boldsymbol{k}_0$. The analogy ends here though, since no transverse motion arises in the Voigt effect.

V. PRACTICAL OBSERVATION

Under normal conditions, the oscillating SHE described here is tenuous for two main reasons. First, because it occurs at the scale k_0^{-1}. Although this scale greatly exceeds the optical wavelength, it remains small compared to the beam width w_0. Second, because the coherent mode attenuates as $\exp(-z/z_s)$ due to multiple scattering.

In practice, the first difficulty can be circumvented by exploiting the principle of weak quantum measurements [7,9,33,34], where one performs a post-selection of the transmitted light along a polarization direction e_{out}. In this configuration, the beam centroid is defined as

$$\langle \boldsymbol{R}(z)\rangle = \frac{\int d\boldsymbol{r}_\perp \boldsymbol{r}_\perp |\langle \boldsymbol{e}_{out}^* \cdot \boldsymbol{E}(\boldsymbol{r}_\perp, z)\rangle|^2}{\int d\boldsymbol{r}_\perp |\langle \boldsymbol{e}_{out}^* \cdot \boldsymbol{E}(\boldsymbol{r}_\perp, z)\rangle|^2}. \qquad (8)$$

To amplify the SHE, the idea is to start from a beam linearly polarized along $\boldsymbol{e}_0 = \hat{\boldsymbol{x}}'$. SOI then split the beam into two parts, whose far tails have finite and opposite helicities. By detecting light using a nearly orthogonal polarizer $\boldsymbol{e}_{out} \propto \hat{\boldsymbol{y}} + i\delta \hat{\boldsymbol{x}}'$ with $|\delta| \ll 1$, one can then select out these tails and amplify the first term in Eq. (4) from k_0^{-1} to w_0. In Appendix C we show that a similar strategy can be used to enhance the second term in Eq. (4), using a post-selection polarizer $\boldsymbol{e}_{out} \propto \hat{\boldsymbol{y}} + \delta \hat{\boldsymbol{x}}'$.

The second difficulty, the attenuation of the coherent mode due to scattering, can on the other hand be overcome by again taking advantage of the disorder correlation. To see how, we show in the inset of Fig. 2 the ratio z_s/z_L of the mean free path to the SOI parameter z_L at smaller values of $k_0\sigma$. We observe that at a given angle $\hat{k}_0$ this ratio reaches a maximum where z_L is of the order of a few z_s only. By properly choosing σ, it is therefore possible to make the SHE appear at a pretty short scale. In Fig. 4, we show several types of transverse trajectories of the coherent mode computed from Eq. (8), by combining the weak measurement technique together with the maximization of z_s/z_L via σ (see Appendix C for the analytical expressions of $\langle \boldsymbol{R}(z)\rangle$ in this configuration). The insets demonstrate the possibility to realize a sizable $R_y(z)$ over distances z/z_s where the coherent mode remains observable.

VI. CONCLUSION

In conclusion, we have shown the existence of an oscillating spin Hall effect in transversally random media, controllable and amplifiable with the disorder correlation. While this phenomenon is visible in the coherent mode after disorder averaging, we expect it to be detectable for a single realization as well provided the beam crosses a material volume much larger than the disorder correlation length. Generally speaking, the control of spin-orbit interactions of light in disorder could be further improved using other degrees of freedom such as scatterer resonances [35] or time-dependent beams [36,37]. Spatio-temporal spin-orbit interactions seem, in particular, a promising direction of research [38–40].
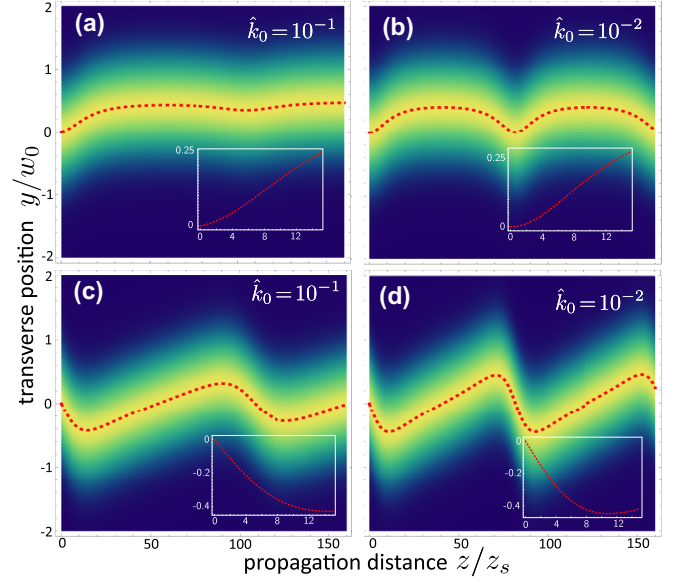
ACKNOWLEDGMENTS

FIG. 4. Normalized intensity of the coherent mode postselected by a polarizer $\boldsymbol{e}_{out}$ ("weak measurement"): $|\langle \boldsymbol{e}_{out}^* \cdot \boldsymbol{E}(\boldsymbol{r}_\perp, z)\rangle|^2 / \int d\boldsymbol{r}_\perp |\langle \boldsymbol{e}_{out}^* \cdot \boldsymbol{E}(\boldsymbol{r}_\perp, z)\rangle|^2$. In panels (a) and (b), $\boldsymbol{e}_{out} \propto \hat{\boldsymbol{y}} + i\delta \hat{\boldsymbol{x}}'$, while in panels (c) and (d), $\boldsymbol{e}_{out} \propto \hat{\boldsymbol{y}} + \delta \hat{\boldsymbol{x}}'$, corresponding to an amplification of the first and second term in Eq. (4), respectively [here $k_0 w_0 = 15$ and $\delta = (k_0 w_0)^{-1}$]. Notice that the SHE is now of the order of the beam width w_0. Dotted curves mark the centroid position $R_y(z)$. Here, $k_0\sigma$ is chosen at the point where the ratio z_s/z_L is maximum (see the inset of Fig. 2): $k_0\sigma = 0.1056$ in panels (a) and (c), $k_0\sigma = 0.01005$ in panels (b) and (d). Insets show zooms of $R_y(z)$ at the scale of a few z_s.

APPENDIX A: DISORDER-AVERAGED FIELD

In this Appendix, we derive the general expression of the average electric field, Eq. (2). To this aim, we rely on the disorder-averaged Green's tensor of the Helmholtz equation (1), $\langle \boldsymbol{G}(\boldsymbol{r}_\perp, z)\rangle$, which we compute by perturbation theory assuming weak disorder. Once $\langle \boldsymbol{G}\rangle$ is known, the electric field follows from

$$\langle \tilde{\boldsymbol{E}}(\boldsymbol{k}_\perp, z)\rangle = 2i\sqrt{k^2 - \boldsymbol{k}_\perp^2} \langle \boldsymbol{G}(\boldsymbol{k}_\perp, z)\rangle \tilde{\boldsymbol{E}}_0(\boldsymbol{k}_\perp). \qquad (A1)$$

The Fourier transform of the Green's tensor with respect to $\boldsymbol{r}_\perp$ and z obeys the Dyson equation

$$\langle \boldsymbol{G}(\boldsymbol{k}_\perp, k_z)\rangle = [\boldsymbol{G}^{(0)}(\boldsymbol{k}_\perp, k_z)^{-1} - \boldsymbol{\Sigma}(\boldsymbol{k}_\perp, k_z)]^{-1}, \qquad (A2)$$

where

$$G_{ij}^{(0)}(\boldsymbol{k}_\perp, k_z) = \frac{\delta_{ij} - \hat{k}_i \hat{k}_j}{k^2 - \boldsymbol{k}_\perp^2 - k_z^2 + i0^+} \qquad (A3)$$

is the Green's tensor of the homogeneous background medium of permittivity $\bar{\epsilon}$. The wave number is $k = \omega/c$, with $c = c_0/\sqrt{\bar{\epsilon}}$. $\hat{k}_i = k_i/k$ refer to the components of the three-dimensional wave vector, and $i = x, y, z$ in the Cartesian basis. In Eq. (A2), the self-energy $\boldsymbol{\Sigma}$ is a 3×3 symmetric matrix. At

weak disorder, it is given by the Born approximation [41]

$$\Sigma_{ij}(\boldsymbol{k}_\perp, k_z) \simeq k^4 \int \frac{d^2 \boldsymbol{k}'_\perp}{(2\pi)^2} \frac{B(\boldsymbol{k}_\perp - \boldsymbol{k}'_\perp)(\delta_{ij} - \hat{k}'_i \hat{k}'_j)}{k^2 - \boldsymbol{k}'^2_\perp - k_z^2 + i0^+}, \quad (A4)$$

where $B(\boldsymbol{k}_\perp - \boldsymbol{k}'_\perp) = \gamma \exp[-\sigma^2(\boldsymbol{k}_\perp - \boldsymbol{k}'_\perp)^2]$ is the disorder power spectrum, i.e., the Fourier transform of the correlator of permittivity fluctuations. To compute the average Green's tensor, it is sufficient to evaluate $\boldsymbol{\Sigma}(\boldsymbol{k}_\perp, k_z)$ for $\boldsymbol{k}_\perp$ aligned with the x axis. In this case, $\Sigma_{xy} = \Sigma_{yz} = 0$. By performing the two tensor inversions in the Dyson equation (A2), we obtain

$$\langle G_{ij}(\boldsymbol{k}_\perp, k_z) \rangle = G_1(\boldsymbol{k}_\perp, k_z)\delta_{ij} - G_2(\boldsymbol{k}_\perp, k_z)\hat{k}_i \hat{k}_j$$
$$+ \frac{1}{\hat{k}_\perp^2}[G_1(\boldsymbol{k}_\perp, k_z) - G_2(\boldsymbol{k}_\perp, k_z)]$$
$$\times (\delta_{iz}\hat{k}_j \hat{k}_z + \delta_{jz}\hat{k}_i \hat{k}_z - \delta_{iz}\delta_{jz} - \hat{k}_i \hat{k}_j), \quad (A5)$$

where

$$G_{1(2)}(\boldsymbol{k}_\perp, k_z) = \frac{1}{k^2 - \boldsymbol{k}_\perp^2 - k_z^2 - \Sigma_{1(2)}(\boldsymbol{k}_\perp, k_z)}, \quad (A6)$$

with $\Sigma_1(\boldsymbol{k}_\perp, k_z) = \Sigma_{yy}$ and $\Sigma_2(\boldsymbol{k}_\perp, k_z) = \Sigma_{xx}(1 - \hat{k}_\perp^2) + \Sigma_{zz}(1 - \hat{k}_z^2) - 2\Sigma_{xz}\hat{k}_x \hat{k}_z$. As explained in the main text, the average Green's tensor here depends on two independent self-energies because the system has a unique spatial symmetry, the conservation of momentum along z. At weak disorder, the parameters $\Sigma_{1(2)}$ are typically small compared to k_0^2. In this limit, the Fourier transform of Eq. (A5) with respect to k_z, $G_{ij}(\boldsymbol{k}_\perp, z) = \int dk_z/(2\pi)G_{ij}(\boldsymbol{k}_\perp, k_z)e^{ik_z z}$, reads

$$\langle G_{ij}(\boldsymbol{k}_\perp, z) \rangle = -i\frac{e^{ik_z z}}{2k_z}\left[e^{-i\Sigma_1 z/2k_z}\delta_{ij} - e^{-i\Sigma_2 z/2k_z}\hat{k}_i \hat{k}_j \right.$$
$$+ \frac{e^{-i\Sigma_1 z/2k_z} - e^{-i\Sigma_2 z/2k_z}}{\hat{k}_\perp^2}$$
$$\left. \times (\delta_{iz}\hat{k}_j \hat{k}_z + \delta_{jz}\hat{k}_i \hat{k}_z - \delta_{iz}\delta_{jz} - \hat{k}_i \hat{k}_j) \right], \quad (A7)$$

where k_z now stands for $(k^2 - \boldsymbol{k}_\perp^2)^{1/2}$. By inserting this expression in Eq. (A1), we finally obtain Eq. (2). Since, for a collimated beam, $\tilde{\boldsymbol{E}}_0(\boldsymbol{k}_\perp)$ is peaked around $\boldsymbol{k}_\perp = \boldsymbol{k}_0$, the self-energies can be evaluated on shell, i.e., approximating $\Sigma_{1(2)} \simeq \Sigma_{1(2)}(\boldsymbol{k}_0, (k^2 - k_0^2)^{1/2})$.

APPENDIX B: SPIN-ORBIT INTERACTION PARAMETERS

The evolution of the beam centroid, Eq. (4), is controlled by the two spin-orbit parameters $z_S = [\text{Im}(\Sigma_2 - \Sigma_1)/k_z]^{-1}$ and $z_L = [\text{Re}(\Sigma_2 - \Sigma_1)/k_z]^{-1}$. To compute them explicitly, one needs the expressions of the self-energies Σ_1 and Σ_2, which follow from Eq. (A4). Using the definitions of Σ_1 and Σ_2 evaluated on shell, we obtain

$$z_L^{-1} = \gamma k^3 \text{ p.v.} \int_0^\infty \frac{\hat{k}_0^2 \alpha \, d\alpha}{4\pi k_0^2 \sigma^2 \sqrt{1 - \hat{k}_0^2(1 - \alpha^2)}} e^{-k_0^2 \sigma^2(1+\alpha^2)}$$
$$\times \left[2k_0^2\sigma^2\left(-2\alpha^2 + \hat{k}_0^2(1 + \alpha^4)\right)I_0\left(2k_0^2\sigma^2\alpha\right) \right.$$
$$\left. + \alpha\left(2 + 4(1 - \hat{k}_0^2)k_0^2\sigma^2\alpha - \hat{k}_0^2\alpha^2\right)I_1\left(2k_0^2\sigma^2\alpha\right) \right] \quad (B1)$$

and

$$z_S^{-1} = \gamma k^3 \frac{\hat{k}_0^2 e^{-2k_0^2\sigma^2}}{8k_0^2\sigma^2\sqrt{1 - \hat{k}_0^2}}\left[4\left(1 - \hat{k}_0^2\right)k_0^2\sigma^2 I_0\left(2k_0^2\sigma^2\right)\right.$$
$$\left. - \left(2 + 4k_0^2\sigma^2 - \hat{k}_0^2\left(1 + 4k_0^2\sigma^2\right)\right)I_1\left(2k_0^2\sigma^2\right) \right], \quad (B2)$$

where I_n is the n-order modified Bessel function of the first kind and p.v. denotes the principal value. Notice that both z_L^{-1} and z_S^{-1} vanish in the paraxial limit $\hat{k}_0 \to 0$, corresponding to $\Sigma_1 \to \Sigma_2$. In this case, spin-orbit corrections to the coherent mode become negligible. We finally provide the explicit expression of the mean free path along z, $z_s = -\text{Im}(\Sigma_1)/k_z$:

$$z_s^{-1} = \gamma k^3 \frac{e^{-2k_0^2\sigma^2}}{4\sqrt{1 - \hat{k}_0^2}}\left[I_0\left(2k_0^2\sigma^2\right) - \frac{\hat{k}_0^2 I_1\left(2k_0^2\sigma^2\right)}{2k_0^2\sigma^2}\right].$$

APPENDIX C: WEAK MEASUREMENT

As in deterministic systems [7,9,33,34], the method of weak quantum measurements makes it possible to amplify the spin Hall effect in a random medium. Here we explain how it can be exploited to selectively amplify both contributions of the coherent mode centroid, Eq. (4). To this aim, we consider an incident beam linearly polarized along $\boldsymbol{e}_0 = \hat{\boldsymbol{x}}'$. With this initial state, we show in Fig. 5 the spatially resolved Stokes parameters of the beam along the transverse direction y at a fixed, finite value of z. These parameters respectively represent the distributions of circularly polarized light,

$$\mathcal{V}(y) = \frac{2\,\text{Im}[\langle E_x^*(x = 0, y, z)\rangle\langle E_y(x = 0, y, z)\rangle]}{\int d\boldsymbol{r}_\perp I_c(\boldsymbol{r}_\perp, z)}, \quad (C1)$$

the distribution of light linearly polarized along the x' or y axes,

$$\mathcal{Q}(y) = \frac{|\langle E_x(0, y, z)\rangle|^2 - |\langle E_y(0, y, z)\rangle|^2}{\int d\boldsymbol{r}_\perp I_c(\boldsymbol{r}_\perp, z)}, \quad (C2)$$

and the distribution of light linearly polarized at $\pm 45°$ in the plane (x', y),

$$\mathcal{U}(y) = \frac{2\,\text{Re}[\langle E_x^*(0, y, z)\rangle\langle E_y(0, y, z)\rangle]}{\int d\boldsymbol{r}_\perp I_c(\boldsymbol{r}_\perp, z)}. \quad (C3)$$

These polarization distributions satisfy $\mathcal{Q}^2 + \mathcal{V}^2 + \mathcal{U}^2 = \mathcal{I}^2$, with

$$\mathcal{I}(y) = \frac{|\langle E_x(0, y, z)\rangle|^2 + |\langle E_y(0, y, z)\rangle|^2}{\int d\boldsymbol{r}_\perp I_c(\boldsymbol{r}_\perp, z)} \quad (C4)$$

the total intensity distribution along y.

We first discuss the case $z_L = \infty$, Fig. 5(a), (configuration A in the main text), where only the first term in the r.h.s. of Eq. (4) is expected. In terms of polarization distributions, this manifests itself by the fact that $\mathcal{U}(y) = 0$. The effect of spin-orbit interactions is then to split a small portion of the incident beam into two components of circularly polarized light with opposite helicity, as described by the $\mathcal{V}$ distribution in Fig. 5(a). By detecting light by means of a nearly orthogonal polarizer $\boldsymbol{e}_{\text{out}} \propto \hat{\boldsymbol{y}} + i\delta\hat{\boldsymbol{x}}'$ with $|\delta| \ll 1$, one can then eliminate the main $\mathcal{Q}$ component, and select out either the positive or negative $\mathcal{V}$ contributions depending on the sign of δ. Spatially, these contributions are typically shifted by the beam width w_0.
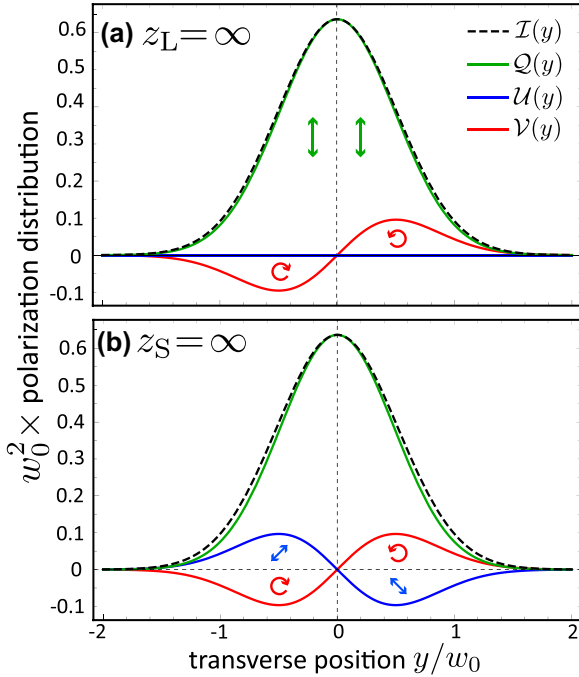
FIG. 5. Spatially resolved Stokes parameters along direction y of a beam prepared with initial polarization $\boldsymbol{e}_0 = \hat{\boldsymbol{x}}'$, after a propagation distance z in the random medium, for $\hat{k}_0 = 0.1$. Axes are normalized using the beam width w_0, and we set $k_0 w_0 = 8$. $\mathcal{I}(y)$ is the total intensity distribution, $\mathcal{Q}(y)$ [resp. $\mathcal{U}(y)$] the distribution of light linearly polarized along $\hat{\boldsymbol{x}}'$ or $\hat{\boldsymbol{y}}$ [resp. $(\hat{\boldsymbol{x}}' \pm \hat{\boldsymbol{y}})/\sqrt{2}$], and $\mathcal{V}(y)$ the distribution of circularly polarized light. Panel (a) corresponds to configuration A ($z_{\mathrm{L}} = \infty$), with $z/z_{\mathrm{S}} = 3\pi$. Panel (b) corresponds to configuration B ($z_{\mathrm{S}} = \infty$), with $z/z_{\mathrm{L}} = -\pi$. The two terms in Eq. (4) can be separately amplified by post-selecting out the $\mathcal{V}$ or $\mathcal{U}$ components, respectively.

Let us now consider the general scenario where z_{L} is finite. In this case, we find that $\mathcal{U}(y)$ is not zero any more, i.e., a small part of the beam further splits into two components linearly polarized along $(\hat{\boldsymbol{x}}' \pm \hat{\boldsymbol{y}})/\sqrt{2}$ during propagation. This case is displayed in Fig. 5(b), in the particular limit $z_{\mathrm{S}} = \infty$ (configuration B in the main text). This more general polarization structure offers the possibility to selectively magnify *either* the first or the second term in Eq. (4), by respectively post-selecting out the $\mathcal{V}$ or $\mathcal{U}$ components. To select and amplify the first term, the procedure is as described above, i.e., one detects the beam using a post-selection polarizer $\boldsymbol{e}_{\mathrm{out}} \propto \hat{\boldsymbol{y}} + i\delta\hat{\boldsymbol{x}}'$. If, on the other hand, one wishes to observe and amplify the second term in Eq. (4), the $\mathcal{U}$ component of the polarization distribution must be selected out. In the same spirit, this can be achieved using a post-selection polarizer $\boldsymbol{e}_{\mathrm{out}} \propto \hat{\boldsymbol{y}} + \delta\hat{\boldsymbol{x}}'$.

The intensity distributions of the coherent mode following the weak measurement post-selection are obtained by inserting Eq. (2) and the definitions of the SOI parameters z_{S} and z_{L} into Eq. (8). This gives the following expressions for the projection of the beam centroid onto the y axis:

$$R_y(z) = -\frac{\delta}{k_0} \frac{1 - e^{-z/2z_{\mathrm{S}}} \cos(z/2z_{\mathrm{L}})}{\delta^2 + \left(\frac{1}{k_0 w_0}\right)^2 |1 - e^{-z/2z_{\mathrm{S}}} e^{iz/2z_{\mathrm{L}}}|^2} \quad \text{(C5)}$$

for $\boldsymbol{e}_{\mathrm{out}} \propto \hat{\boldsymbol{y}} + i\delta\hat{\boldsymbol{x}}'$ [amplification of the first term in Eq. (4)], and

$$R_y(z) = \frac{\delta}{k_0} \frac{e^{-z/2z_{\mathrm{S}}} \sin(z/2z_{\mathrm{L}})}{\delta^2 + \left(\frac{1}{k_0 w_0}\right)^2 |1 - e^{-z/2z_{\mathrm{S}}} e^{iz/2z_{\mathrm{L}}}|^2} \quad \text{(C6)}$$

for $\boldsymbol{e}_{\mathrm{out}} \propto \hat{\boldsymbol{y}} + \delta\hat{\boldsymbol{x}}'$ [amplification of the second term in Eq. (4)]. The intensity distributions shown in Fig. 4 finally follow from $|\langle \boldsymbol{e}_{\mathrm{out}}^* \cdot \boldsymbol{E}(\boldsymbol{r}_\perp, z)\rangle|^2 / \int d\boldsymbol{r}_\perp |\langle \boldsymbol{e}_{\mathrm{out}}^* \cdot \boldsymbol{E}(\boldsymbol{r}_\perp, z)\rangle|^2 \propto \exp[-(y - R_y(z))^2/w_0^2]$.

[1] K. Y. Bliokh, F. J. Rodríguez-Fortuño, F. Nori, and A. Zayats, Spin-orbit interactions of light, Nat. Photonics **9**, 796 (2015).

[2] F. Cardano, L. Marrucci, Spin-orbit photonics, Nat. Photonics **9**, 776 (2015).

[3] A. Aiello, P. Banzer, M. Neugebauer, and G. Leuchs, From transverse angular momentum to photonic wheels, Nat. Photonics **9**, 789 (2015).

[4] J. Wunderlich, B.-G. Park, A. C. Irvine, L. P. Zârbo, E. Rozkotová, P. Nemec, V. Novák, J. Sinova, and T. Jungwirth, Spin Hall effect transistor, Science **330**, 1801 (2010).

[5] D. Awschalom and M. Flatté, Challenges for semiconductor spintronics, Nat. Phys. **3**, 153 (2007).

[6] X. Ling, X. Zhou, K. Huang, Y. Liu, C.-W. Qiu, H. Luo, and S. Wen, Recent advances in the spin Hall effect of light, Rep. Prog. Phys. **80**, 066401 (2017).

[7] O. Hosten and P. Kwiat, Observation of the spin Hall effect of light via weak measurements, Science **319**, 787 (2008).

[8] Y. Qin, Y. Li, H. He, and Q. Gong, Measurement of spin Hall effect of reflected light, Opt. Lett. **34**, 2551 (2009).

[9] Y. Gorodetski, K. Y. Bliokh, B. Stein, C. Genet, N. Shitrit, V. Kleiner, E. Hasman, and T. W. Ebbesen, Weak Measurements of Light Chirality with a Plasmonic Slit, Phys. Rev. Lett. **109**, 013901 (2012).

[10] K. Y. Bliokh, A. Niv, V. Kleiner, and E. Hasman Geometrodynamics of spinning light, Nat. Photonics **2**, 748 (2008).

[11] D. Haefner, S. Sukhov, and A. Dogariu, Spin Hall Effect of Light in Spherical Geometry, Phys. Rev. Lett. **102**, 123903 (2009).

[12] O. G. Rodríguez-Herrera, D. Lara, K. Y. Bliokh, E. A. Ostrovskaya, and C. Dainty, Optical Nanoprobing via Spin-Orbit Interaction of Light, Phys. Rev. Lett. **104**, 253601 (2010).

[13] B. Roy, N. Ghosh, A. Banerjee, S. D. Gupta, and S. Roy, Manifestations of geometric phase and enhanced spin Hall shifts in an optical trap, New J. Phys. **16**, 083037 (2014).

[14] A. V. Dooghin, N. D. Kundikova, V. S. Liberman, and B. Y. Zel'dovich, Optical Magnus effect, Phys. Rev. A **45**, 8204 (1992).

[15] V. S. Liberman and B. Y. Zel'dovich, Spin-orbit interaction of a photon in an inhomogeneous medium, Phys. Rev. A **46**, 5199 (1992).

[16] K. Y. Bliokh and Y. P. Bliokh, Modified geometrical optics of a smoothly inhomogeneous isotropic medium: The anisotropy, Berry phase, and the optical Magnus effect, Phys. Rev. E **70**, 026605 (2004).

[17] M. Onoda, S. Murakami, and N. Nagaosa, Hall Effect of Light, Phys. Rev. Lett. **93**, 083901 (2004).

[18] T. Bardon-brun, D. Delande, and N. Cherroret, Spin Hall Effect of Light in a Random Medium, Phys. Rev. Lett. **123**, 043901 (2019).

[19] I. M. Vellekoop and A. P. Mosk, Focusing coherent light through opaque strongly scattering media, Opt. Lett. **32**, 2309 (2007).

[20] S. Popoff, G. Lerosey, M. Fink, A. C. Boccara, and S. Gigan, Image transmission through an opaque material Nat. Commun. **1**, 81 (2010).

[21] I. M. Vellekoop, A. Lagendijk, and A. P. Mosk, Exploiting disorder for perfect focusing, Nat. Photonics **4**, 320 (2010).

[22] O. Katz, E. Small, and Y. Silberberg, Looking around corners and through thin turbid layers in real time with scattered incoherent light, Nat. Photon. **6**, 549 (2012).

[23] O. Katz, P. Heidmann, M. Fink, and S. Gigan, Noninvasive single-shot imaging through scattering layers and around corners via speckle correlations Nat. Photonics **8**, 784 (2014).

[24] S. Rotter and S. Gigan, Light fields in complex media: Mesoscopic scattering meets wave control, Rev. Mod. Phys. **89**, 015005 (2017).

[25] T. Schwartz, G. Bartal, S. Fishman, and M. Segev, Transport and Anderson localization in disordered two-dimensional photonic lattices, Nature (London) **446**, 52 (2007).

[26] M. Boguslawski, S. Brake, D. Leykam, A. S. Desyatnikov, and C. Denz, Observation of transverse coherent backscattering in disordered photonic structures Sci. Rep. **7**, 10439 (2017).

[27] N. Cherroret, Coherent multiple scattering of light in (2+1) dimensions, Phys. Rev. A **98**, 013805 (2018).

[28] M. Bellec, P. Panagiotopoulos, D. G. Papazoglou, N. K. Efremidis, A. Couairon, and S. Tzortzakis, Observation and Optical Tailoring of Photonic Lattice Filaments, Phys. Rev. Lett. **109**, 113905 (2012).

[29] P. Sheng, *Introduction to Wave Scattering, Localization, and Mesoscopic Phenomena* (Academic Press, San Diego, 1995).

[30] Equation (4) holds at leading order in $\hat{k}_0^2$. At arbitrary value of $\hat{k}_0$, the expression remains correct provided the $1/k_0$ prefactors are replaced by $(1 - \hat{k}_0^2)^{1/2}/k_0$. This implies that SOI also show up at large angle of incidence, although their amplitude tends to decrease when approaching the regime of grazing incidence.

[31] D. L. Andrews and M. Babiker, *The Angular Momentum of Light* (Cambridge University Press, Cambridge, 2013).

[32] D. Budker, W. Gawlik, D. F. Kimball, S. M. Rochester, V. V. Yashchuk, and A. Weis, Resonant nonlinear magneto-optical effects in atoms, Rev. Mod. Phys. **74**, 1153 (2002).

[33] J. Dressel, M. Malik, F. M. Miatto, A. N. Jordan, and R. W. Boyd, *Colloquium*: Understanding quantum weak values: Basics and applications, Rev. Mod. Phys. **86**, 307 (2014).

[34] M. R. Dennis and J. B. Götte, The analogy between optical beam shifts and quantum weak measurements, New J. Phys. **14**, 073013 (2012).

[35] A. Lagendijk and B. A. van Tiggelen, Resonant multiple scattering of light, Phys. Rep. **270**, 143 (1996).

[36] M. Chalony, R. Pierrat, D. Delande, and D. Wilkowski, Coherent flash of light emitted by a cold atomic cloud, Phys. Rev. A **84**, 011401(R) (2011).

[37] C. C. Kwong, T. Yang, M. S. Pramod, K. Pandey, D. Delande, R. Pierrat, and D. Wilkowski, Cooperative Emission of a Coherent Superflash of Light, Phys. Rev. Lett. **113**, 223601 (2014).

[38] S. W. Hancock, S. Zahedpour, A. Goffin, and H. M. Milchberg, Free-space propagation of spatiotemporal optical vortices, Optica **6**, 1547 (2019).

[39] A. Chong, C. Wan, J. Chen, and Q. Zhan, Generation of spatiotemporal optical vortices with controllable transverse orbital angular momentum, Nat. Photonics **14**, 350 (2020).

[40] K. Y. Bliokh, Spatiotemporal Vortex Pulses: Angular Momenta and Spin-Orbit Interaction, Phys. Rev. Lett. **126**, 243601 (2021).

[41] E. Akkermans and G. Montambaux, *Mesoscopic Physics of Electrons and Photons* (Cambridge University Press, Cambridge, 2007).